Universität Regensburg
Mathematik

Multiple scales in phase separating systems with elastic misfit

Harald Garcke, Martin Lenz, Barbara Niethammer, Martin Rumpf and Ulrich Weikard

Multiple scales in phase separating systems with elastic misfit

Harald Garcke[1], Martin Lenz[2], Barbara Niethammer[3], Martin Rumpf[2], and Ulrich Weikard[4]

[1] NWF I – Mathematik, Universität Regensburg, 93040 Regensburg
[2] Institut für Numerische Simulation, Rheinische Friedrich-Wilhelms-Universität Bonn, Nußallee 15, 53115 Bonn
[3] Institut für Mathematik, Humboldt-Universität zu Berlin, Unter den Linden 6, 10099 Berlin
[4] Fachbereich Mathematik, Gerhard-Mercator-Universität Duisburg, Lotharstr. 63/65, 47048 Duisburg

harald.garcke@mathematik.uni-regensburg.de,
martin.lenz@ins.uni-bonn.de, niethamm@mathematik.hu-berlin.de,
martin.rumpf@ins.uni-bonn.de, weikard@math.uni-duisburg.de

1 Introduction

In this article we review recent attempts to understand the interaction of different length and time scales in phase separating systems with elastic misfit. Phase separation occurs for example if an alloy is quenched below a critical temperature, where a homogeneous mixture of the alloy components is not stable. The early stage of the separation process, where different phases, characterized by the respective concentrations of the alloy components, appear is called spinodal decomposition.

The Cahn–Hilliard model [CH58] and its extension with elasticity, the Cahn–Larché model [CL82, CL73], have originally been introduced to model spinodal decomposition. Later numerical simulations (see e.g. [Ell89]) and formally matched asymptotic expansions (see [Pe89]) showed that the Cahn–Hilliard equation can also describe a process on a slower intermediate time scale in which the regions occupied by the phases rearrange in order to decrease their free energy. In the case that elastic contributions can be neglected, the free energy is essentially given by the surface energy and the evolution leads to nearly spherical disjoint components, called particles (see Fig. 1.1). If anisotropic elastic effects are present the shapes resemble the anisotropy of the elastic energy (see Fig. 1.2).

In the late stage, when the system has already minimized its energy locally, interactions between particles become important. In the case that no
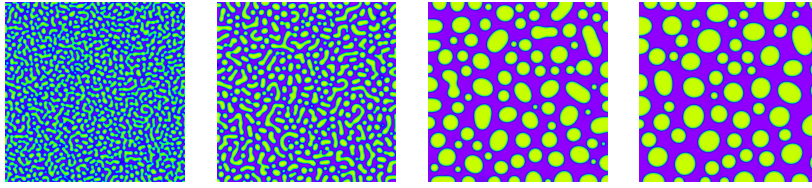
Fig. 1.1. Evolution starting from a perturbation of a uniform state
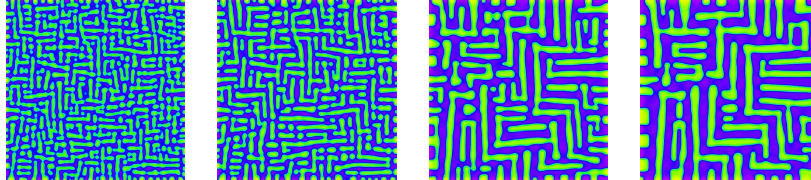
Fig. 1.2. Alignment of interfaces driven by homogeneous, anisotropic elasticity

elastic energy is relevant, small particles shrink, while larger ones grow, a coarsening process known as Ostwald Ripening. The influence of elastic interactions, e.g. through an elastic misfit due to different lattice constants, can drastically influence the coarsening process. The shape of the particles changes from spherical to cuboidal or plate shape, particles can align or even split. In particular on the large time scale the elastic energy which scales like a volume becomes comparable to the surface energy and it might be possible to stabilize the coarsening process ("inverse coarsening"). For a review on the modelling of phase separation in alloys with elastic misfit we refer to [FPL99]. To model the late stage regime, often so called sharp interface models are used, which also appear as singular limits of the Cahn–Hilliard equation (see [GK06]). In contrast to the latter, the boundary between different phases is given by a hypersurface.

In this overview we will discuss both the Cahn–Hilliard equation with elasticity (the Cahn–Larché system) and a Mullins–Sekerka type model with anisotropic and inhomogeneous elasticity. Although we will also discuss some aspects of modelling and mathematical analysis, our main focus will be on computational aspects.

First, we will introduce the governing models and their interpretation as a gradient flow in Sect. 2. The latter will be relevant for the set up of a reduced model to simulate large particle ensembles. In Sect. 3 we study the effect of elastic contributions on spinodal decomposition within the Cahn–Larché model. In Sect. 4 we will explain how the Cahn–Larché system can be solved efficiently and present computational results for the Cahn–Hilliard equation and the Cahn–Larché system. In Sect. 5 we study coarsening rates for a large system of particles. Here we observe a transient coarsening behaviour in the

Cahn–Hilliard model without elasticity and we will also see effects of elasticity on the ripening process.

In Sect. 6 we introduce a boundary integral formulation of the Mullins–Sekerka evolution and a corresponding boundary integral method. Simulations for systems with a few particles will be presented, which in particular show typical particle shapes and display when a certain pattern such as alignment of particles appears. Finally, in Sect. 7, we will use the gradient-flow perspective for the Mullins–Sekerka evolution to derive a reduced model, in which particle shapes are extremely simple. With this approach we can efficiently simulate larger particle systems.

2 The models

2.1 The Cahn–Larché model

We consider the case of a binary alloy, i.e. two alloy components are present with concentrations c_1 and c_2. We choose the concentration difference $c = c_1 - c_2$ as variable which due to the constraint $c_1 + c_2 = 1$ determines the concentrations. The deformation field is denoted by u and since we consider models that are based on linearized elasticity we introduce the linearized strain tensor

$$\varepsilon(F) := \frac{1}{2}(F + F^T), \text{ with } F = \nabla u.$$

The free energy of the system is then given by

$$\mathcal{E}[c, u] = \int_\Omega \{\frac{\gamma}{2}|\nabla c|^2 + \psi(c) + W(c, \nabla u)\} \, dx \tag{2.1}$$

where $\Omega \subset \mathbf{R}^d$ is a bounded domain, $\gamma > 0$ is a small interfacial parameter, $\psi : \mathbf{R} \to \mathbf{R}$ is the non-convex free energy density and $W : \mathbf{R} \times \mathbf{R}^{d \times d} \to \mathbf{R}$ is the elastic energy density. A homogeneous free energy density ψ for a mean field model at a fixed absolute temperature is

$$\psi(c) = \frac{R\theta}{2} \left\{ (1 + c) \ln(1 + c) + (1 - c) \ln(1 - c) \right\} + \frac{R\theta_c}{2}(1 - c^2). \tag{2.2}$$

Here θ_c is the critical temperature and R is the gas constant scaled by the (constant) molar volume. For θ below the critical temperature θ_c the energy density ψ has two global minima c_-, c_+ and hence a non-convex form. For shallow quenches, i.e. $0 \ll \theta < \theta_c$ one usually takes a smooth approximation to (2.2) of the form

$$\psi(c) = b(c^2 - a^2)^2 \ , \quad 0 < a < 1, \ b > 0. \tag{2.3}$$

As elastic energy density W we take a quadratic function in the strain tensor ε and set

$$W(c, \nabla u) = \frac{1}{2}(\varepsilon(\nabla u) - \overline{\varepsilon}(c)) : C(c)(\varepsilon(\nabla u) - \overline{\varepsilon}(c)).$$

Here $\overline{\varepsilon}(c)$ is the symmetric misfit strain (also called eigenstrain), $C(c)$ is the fourth rank elasticity tensor and $A : B := tr(A^T B)$ for linear mappings A and B. As the elasticity tensor C is assumed to be symmetric and positive definite we obtain that $\overline{\varepsilon}(c)$ is the energetically favourable and hence stress free strain at concentration c. Typically $\overline{\varepsilon}$ is affine linear, i.e.

$$\overline{\varepsilon}(c) = \varepsilon^1 + \varepsilon^* c$$

where $\varepsilon^1, \varepsilon^* \in \mathbf{R}^{d \times d}$ are symmetric. We allow for an elasticity tensor that can be different for the two components and hence C can depend on the concentration c.

For an isotropic material we obtain

$$C(c)\varepsilon = 2\mu(c)\varepsilon + \lambda(c)\, tr(\varepsilon)\mathrm{Id}$$

where the Lamé moduli μ and λ depend on the concentration c.

For a material with cubic symmetry we have

$$C(c)\varepsilon = 2\mu(c)\varepsilon + \lambda(c)\, tr\, \varepsilon \mathrm{Id} + \mu'(c)\mathrm{diag}\, \varepsilon$$

where $\mathrm{diag}\,\varepsilon$ is the matrix that one obtains, if all off-diagonal entries are set to zero. In general C is an arbitrary fourth rank tensor $C(c) = (C_{ij\,i'j'}(c))$ and using the symmetry conditions

$$C_{ij\,i'j'} = C_{ij\,j'i'} = C_{ji\,i'j'} = C_{i'j'\,ij}$$

one can compute that for $d = 3$ there are 21 degrees of freedom in C which of course in general will be restricted by crystal symmetry.

For example in a cubic system we obtain that $C_{1111} = C_{2222} = C_{3333}$, $C_{iijj} = C_{ii\kappa\kappa}$ (for i, j, κ mutually different), $C_{2323} = C_{3131} = C_{1212}$ and all other entries in C either follow from the above by symmetry or they are zero. Sometimes a fourth rank tensor in $\mathbf{R}^3$ is denoted by C_{ij} (Voigt notation). In this case the indices i, j take values $1, 2, 3, 4, 5, 6$ and they stand for the pairs $11, 22, 33, 23, 31, 12$ in the original notation. This means in a cubic system we only need to specify C_{11}, C_{12} and C_{44}. All other parameters are determined by symmetry. For a discussion of other symmetry classes we refer to Gurtin [Gu72]. We will also always assume that $C(c)$ is positive definite and bounded uniformly in c.

Taking mechanical effects in the Cahn–Hilliard model into account we obtain the system

$$\partial_t c = \Delta w, \tag{2.4}$$

$$w = \frac{\delta \mathcal{E}}{\delta c} = -\gamma \Delta c + \psi'(c) + W_{,c}(c, \nabla u), \tag{2.5}$$

$$0 = \frac{\delta \mathcal{E}}{\delta u} = -\nabla \cdot W_{,F}(c, \varepsilon(\nabla u)), \tag{2.6}$$

which we sometimes also call the Cahn–Larché system (see [CL82, CL73]). Here $\frac{\delta E}{\delta c}$ denotes the first variation of E with respect to c and $W_{,c}$ is the partial derivative with respect to c (the same notation holds with respect to u). We remark that for simplicity in (2.4) the mobility is taken to be 1. The chemical potential w is the diffusion potential and is given by the first variation of energy with respect to concentration. The quantity $S = W_{,F}$ with $F = \nabla u$ is the stress and hence (2.6) are the mechanical equilibrium equations from the theory of elasticity.

The set of equations then has to be completed by appropriate boundary conditions which can be e.g. periodic boundary conditions or Neumann boundary conditions for w and c and a prescribed normal stress at the boundary for the u–equation.

2.2 The Cahn–Larché system as a gradient flow

The Cahn–Larché system can be viewed as a gradient flow. A gradient flow is the flow in the direction of steepest descent in an energy landscape. This framework requires a differentiable manifold $\mathcal{M}$, and a vector field f, which attaches a tangent vector $f(x) \in T_x\mathcal{M}$ to every point $x \in \mathcal{M}$. The vector field f defines a dynamical system $\dot{x} = f(x)$. A gradient flow is a dynamical system where f is the negative gradient $-\mathrm{grad}\,\mathcal{E}$ of a function $\mathcal{E}$ on $\mathcal{M}$. The notion of a gradient requires a Riemannian structure, that is, a metric tensor g on $\mathcal{M}$. Then, the precise formulation of $\dot{x} = -\mathrm{grad}\,\mathcal{E}_x$ is

$$g_{x(t)}(\dot{x}(t), y) + \langle \mathrm{diff}\,\mathcal{E}_{x(t)}, y \rangle = 0 \quad \text{for all } y \in T_{x(t)}\mathcal{M} \text{ and for all } t. \qquad (2.7)$$

If we choose $y = \dot{x}(t)$ we observe that the value of $\mathcal{E}$ decreases along trajectories.

We now give two possibilities to view the Cahn–Larché system as a gradient flow. First we choose

$$\mathcal{M} := \left\{ c : \Omega \to \mathbf{R} \,\middle|\, \int_\Omega c \, dx = \int_\Omega c_0 \, dx \right\},$$

where $c_0 : \Omega \to \mathbf{R}$ is the concentration at time zero. The tangent space is then given as

$$T_c\mathcal{M} := \left\{ v : \Omega \to \mathbf{R} \,\middle|\, \int_\Omega v \, dx = 0 \right\}$$

and the metric tensor on $T_c\mathcal{M}$ is given by the H^{-1} norm, that is

$$g_c(v, \tilde{v}) := \int_\Omega \nabla \mu_v \cdot \nabla \mu_{\tilde{v}} \, dx$$

where μ_v (respectively $\mu_{\tilde{v}}$) has mean value zero and fulfills

$$\int_\Omega \nabla \mu_v \cdot \nabla \xi \, dx = \int_\Omega v \, \xi \, dx \quad \text{for all} \quad \xi \in H^1(\Omega).$$

We remark that

$$g_c(v, \tilde{v}) = \int_\Omega \mu_v \tilde{v} \, dx.$$

In what follows we will write $\mu_v = (-\Delta)^{-1} v$.

We define

$$\mathcal{E}(c) = \int_\Omega \{\frac{\gamma}{2}|\nabla c|^2 + \psi(c)\} \, dx + \min_u \int_\Omega W(c, \nabla u) \, dx \qquad (2.8)$$

and claim that

$$\langle \operatorname{diff} \mathcal{E}(c), \tilde{v} \rangle = \int_\Omega \{-\gamma \Delta c + \psi'(c) + W_{,c}(c, \nabla u_c)\} \tilde{v} \, dx$$

where u_c solves (2.6) for given c. It should be remarked that the last term in (2.8) can be written as $\int_\Omega W(c, \nabla u_c) \, dx$ which means that also u depends on c. Since (2.6) holds it can be computed that this dependence gives no contribution to the differential. We now obtain that

$$\langle \operatorname{diff} \mathcal{E}, \tilde{v} \rangle = g_c(\partial_t c, \tilde{v}) = \int_\Omega (-\Delta)^{-1} \partial_t c \, \tilde{v} \, dx$$

is equivalent to (2.4)–(2.5) if we set $w := (-\Delta)^{-1} \partial_t c$.

Another gradient flow perspective for the Cahn–Larché system uses the energy (2.1) and uses the manifold

$$\mathcal{M} := \left\{(c, u) : \Omega \to \mathbf{R} \times \mathbf{R}^d \,\middle|\, \int_\Omega c = \int_\Omega c_0 + \text{ boundary conditions for } u\right\}$$

with a corresponding tangent space $T_{(c,u)}\mathcal{M}$. The metric tensor is then chosen to be degenerate with respect to u. In fact we choose

$$g_{(c,u)}((v, w), (\tilde{v}, \tilde{w})) = \int_\Omega \nabla \mu_v \cdot \nabla \mu_{\tilde{v}} \, dx$$

with μ_v and $\mu_{\tilde{v}}$ as above.

We remark that the gradient flow property has been used in Garcke [Ga03b] to show existence of solutions to the Cahn–Larché system.

2.3 The Mullins–Sekerka evolution

In the Mullins–Sekerka model the interface between two phases is described by the boundary $\partial\{\chi = 1\}$, where χ is the characteristic function of one of the phases. We restrict our presentation to the case $\Omega = \mathbf{R}^d$.

The evolution is driven by the reduction of an energy, which is given by

$$\mathcal{E}[\chi, u] := \int_{\mathbf{R}^d} |\nabla \chi| + \int_{\mathbf{R}^d} W(\chi, \nabla u) \, dx,$$

where $\int_{\mathbf{R}^d} |\nabla \chi|$ denotes the perimeter of the set $\{\chi = 0\}$ in $\mathbf{R}^d$. That is, the energy is the sum of interfacial area, which is due to surface tension, and an elastic part, which depends on χ and the deformation field u. In the following we consider linearized elasticity, that is we take

$$W(\chi, F) := \chi W_1(F) + (1 - \chi) W_0(F),$$

$$W_\alpha(F) := \frac{1}{2} C^\alpha (\varepsilon(F) - \bar{\varepsilon}_\alpha) : (\varepsilon(F) - \bar{\varepsilon}_\alpha),$$

in particular, we allow as above that the elasticity tensor is anisotropic as well as inhomogeneous, i.e. different in each phase; and we allow for a misfit between the two phases, $\bar{\epsilon}_1 \neq \bar{\epsilon}_0$. The misfit may also be anisotropic, i.e. it is not necessarily a multiple of the identity.

The evolution of the interface is driven by the gradient of the chemical potential μ, that is the normal velocity v is given by

$$v = [\partial_\nu \mu] \qquad \text{on the interface } \Gamma := \partial \{\chi = 1\}, \tag{2.9}$$

where ν is the outer normal on $\partial \{\chi = 1\}$, and

$$[\partial_\nu \mu] := \lim_{x \to \Gamma, x \in \{\chi = 0\}} \partial_\nu \mu - \lim_{x \to \Gamma, x \in \{\chi = 1\}} \partial_\nu \mu$$

denotes the jump of the normal component of the gradient across the interface. The chemical potential μ is determined for each time t via

$$-\Delta \mu = 0 \qquad\qquad \text{in the bulk } \mathbf{R}^d \backslash \Gamma, \tag{2.10}$$

$$\mu = \kappa + \nu \cdot [E(u)] \nu \qquad \text{on } \Gamma, \tag{2.11}$$

where the jump of the Eshelby tensor

$$E(\chi, F) := W(\chi, F) \mathbf{1} - F^T \frac{\partial W}{\partial F}(\chi, F) \tag{2.12}$$

can be computed from the solution of the elastic equation (see below in (2.13), (2.14)).

We assume that the mechanical fields relax at each time t instantaneously to equilibrium, which yields

$$\operatorname{div} \sigma = 0, \qquad \text{in } \mathbf{R}^d \backslash \Gamma, \tag{2.13}$$

$$[\sigma \cdot \nu] = 0, \qquad \text{on } \Gamma. \tag{2.14}$$

Here, σ denotes the stress tensor, which is given by $\sigma = \frac{\partial W}{\partial F}(\chi, \nabla u)$.

2.4 The Mullins–Sekerka evolution as a gradient flow

We now argue that also the Mullins–Sekerka free boundary problem formally fits into the gradient flow framework: $\mathcal{M}$ has to be chosen as the manifold of all sets, representing the particle phase, with fixed volume, i.e.

$$\mathcal{M} := \left\{ \chi : \mathbf{R}^d \to \{0,1\} \,\middle|\, \int_{R^d} \chi \, dx = \mathcal{V} \,, \, \mathrm{supp}\chi \subset\subset \mathbf{R}^d \right\} .$$

The tangent space $T_\chi \mathcal{M}$ can be described by all admissible normal velocities of Γ, that is

$$T_\chi \mathcal{M} := \left\{ v : \Gamma \to \mathbf{R} \,\middle|\, \int_\Gamma v \, d\mathcal{H}^{d-1} = 0 \right\} .$$

The metric tensor is given here by the H^{-1} norm in the bulk. More precisely

$$g_\chi(v, \tilde{v}) := \int_{\mathbf{R}^d} \nabla \mu_v \cdot \nabla \mu_{\tilde{v}} \, dx \,,$$

where μ_v (respectively $\mu_{\tilde{v}}$) is the bounded solution of the elliptic problem

$$-\Delta \mu_v = 0 \quad \text{in} \quad \mathbf{R}^d \backslash \Gamma \,, \tag{2.15}$$

$$[\nabla \mu_v \cdot \nu] = v \quad \text{on } \Gamma \,. \tag{2.16}$$

After an integration by parts we obtain

$$g_\chi(v, \tilde{v}) = \int_\Gamma -\mu_v \tilde{v} \, d\mathcal{H}^{d-1}.$$

Our assumption in the previous chapter was that we have a clear separation of time scales such that the mechanical fields can be assumed to relax instantaneously to equilibrium given a phase distribution χ. Thus, we replace our energy by

$$\mathcal{E}(\chi) = \int |\nabla \chi| + \min_u \int_{\mathbf{R}^d} W(\chi, \nabla u) \, dx \,.$$

Indeed, it follows that $\min_u \int_{\mathbf{R}^d} W(\chi, \nabla u) \, dx = \int_{\mathbf{R}^d} W(\chi, \nabla u_\chi) \, dx$, where u_χ solves (2.13), (2.14) for given χ.

We have now all the ingredients for a gradient flow evolution at hand. In order to compute it explicitly we have to calculate the differential of $\mathcal{E}$.

First, we recall the well-known result that the first variation of surface area is the mean curvature, that is for $\tilde{\mathcal{E}}(\chi) := \int |\nabla \chi|$ we have

$$\langle \mathrm{diff} \tilde{\mathcal{E}}, \tilde{v} \rangle = \int_\Gamma \kappa \, \tilde{v} \, d\mathcal{H}^{d-1}$$

for all $\tilde{v} \in T_\chi \mathcal{M}$. The differential of the elastic part of the energy is (compare [Ga03a])

$$\langle \mathrm{diff} \hat{\mathcal{E}}, \tilde{v} \rangle = \frac{d}{d\delta} \hat{\mathcal{E}}[\chi_\delta]|_{\delta=0}$$

$$= \int_\Gamma \left(W(\chi, \nabla u) \mathbf{1} - (\nabla u)^T \frac{\partial W}{\partial F}(\chi, \nabla u) \right) \nu \cdot \nu \tilde{v} \, d\mathcal{H}^{d-1} \,.$$

The part in brackets is again the Eshelby tensor $E(\chi, \nabla u)$ (2.12), and the jump of its normal part across the interface is the contribution of the elastic energy to the evolution of the particles.

Therefore we have for the gradient flow, evaluating (2.7), that

$$0 = g_\chi(v, \tilde{v}) + \langle \text{diff}\,\mathcal{E}, \tilde{v} \rangle \;=\; \int_\Gamma (\kappa + \nu \cdot [E(\chi, \nabla u)]\nu - \mu_v)\,\tilde{v}\,d\mathcal{H}^{d-1} \quad (2.17)$$

for all $\tilde{v} \in T_\chi\mathcal{M}$. We see in fact that for the direction of steepest descent the corresponding potential satisfies – up to an irrelevant additive constant – the Gibbs–Thomson law with elasticity (2.11).

3 Spinodal decomposition

At high temperatures the free energy ψ is convex and hence a homogeneous state is stable. If now the system is quenched below the critical temperature θ_c the homogeneous state becomes unstable and different phases form which can be distinguished by a different chemical concentration. This process happens on a very short time scale and the regions with different phases have sizes which are given by a small length scale. If the elasticity tensor or the eigenstrains are anisotropic, one will observe that the phase regions orientate themself in certain directions (see [GMW03],[GRW01]) for numerical simulations). We will now describe how one can make these observations quantitative. We first solve the linearized Cahn–Larché system with the help of Fourier transformation (see Khachaturyan [Kha83]). Then a method developed by Maier-Paape and Wanner allows to show that one will see certain patterns after spinodal decomposition with a probability close to one for the nonlinear evolution (we refer to Garcke, Maier-Paape and Weikard [GMW03] for details). We will assume here that C does not depend on c which is the elastically homogeneous case.

Linearization of the Cahn–Larché system around a constant stationary state $(c, u) = (c_m, 0)$, where $c_m \in \mathbf{R}$ is constant, gives

$$\partial_t c = (-\Delta)(\gamma \Delta c - \psi''(c_m)c + \varepsilon^* : S), \quad (3.1)$$

$$\nabla \cdot S = 0, \quad (3.2)$$

$$S = C(\varepsilon(\nabla u) - \varepsilon^* c). \quad (3.3)$$

We consider the system (3.1)–(3.3) on $\Omega = (0, 2\pi) \times \cdots \times (0, 2\pi)$ with periodic boundary conditions. For a given c we can compute u from (3.2)–(3.3) by Fourier transformation and we can express $\varepsilon^* : S$ as a function in c. The result will be denoted as

$$\mathcal{L}(c) = \varepsilon^* : S.$$

For

$$\varphi_\kappa(x) = \mathrm{e}^{\mathrm{i}\kappa \cdot x}, \quad \mathbf{i} \;\; \text{being the imaginary unit,}$$

with

$$\kappa = (\kappa_1, \dots, \kappa_d) \in \mathbf{Z}^d$$

one obtains (see [Kha83, GMW03])

$$\mathcal{L}(\varphi_\kappa) = L(\kappa)\varphi_\kappa$$

with

$$L(\kappa) = \varepsilon^* : (C[Z(\kappa)S^*\kappa\kappa^T] - S^*)$$

where $S^* := C[\varepsilon^*]$ and $Z(\kappa)$ is the inverse of

$$Z^{-1}(\kappa) = \left(\sum_{j,m}^{d} C_{ijmn}\kappa_j\kappa_m \right)_{i,n=1,\dots,d}.$$

An important observation is that L is homogeneous of degree 0 which implies that $\mathcal{L}$ is a pseudo-differential operator of order 0. The function L can be computed more explicitly in certain cases, e.g. if C is isotropic or has a cubic symmetry (see [GMW03]). In the particular case of cubic symmetry one obtains that certain directions $\kappa \in \mathbf{Z}^d$ are stronger amplified by L than others. This has important consequences for (3.1)–(3.3). If we consider solutions to (3.1)–(3.3) of the separation of variables form

$$c(x,t) = f(t)e^{\mathbf{i}\kappa \cdot x},$$

we obtain

$$f(t) = \alpha e^{\lambda_{\kappa,\gamma} t}, \ \alpha \in \mathbf{R},$$

with

$$\lambda_{\kappa,\gamma} = |\kappa|^2 (-\gamma|\kappa|^2 - \psi''(c_m) + L(\kappa)).$$

If c_m is such that $\psi''(c_m) < 0$, one obtains in the case without elasticity that all κ with a certain wave length are amplified the most. Now in case of anisotropic elasticity also the direction of κ plays an important role when we want to determine the most unstable waves. It turns out (see [Kha83, GMW03] and the references therein) that in case of cubic anisotropy either directions parallel to the coordinate axes or directions parallel to the diagonals of the coordinate axes are amplified more by the influence of elastic interactions. Which of the two cases occur depends on the parameter $\Delta C := C_{11} - C_{12} - 2C_{44}$. One speaks of positive anisotropy if $\Delta C > 0$ and of negative anisotropy if $\Delta C < 0$.

We will demonstrate this for the case of negative anisotropy. In Fig. 3.1 we show the most amplified eigenmodes and a typical function which is a linear combination of basis functions with these eigenmodes. In Fig. 3.2 we show a typical solution of the Cahn–Larché system after spinodal decomposition. We show the modulus of the Fourier coefficients and the sign of the concentration difference in the case of cubic negative anisotropy. One clearly sees the cubic anisotropy which is in contrast to the isotropic case where patterns do not
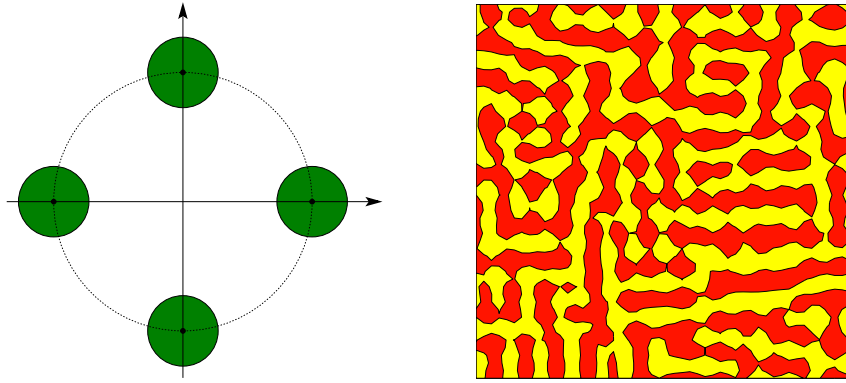
Fig. 3.1. The most amplified eigenmodes in the (κ_1, κ_2)–plane (left) and a typical pattern (right) for negative anisotropy ($\Delta C < 0$)
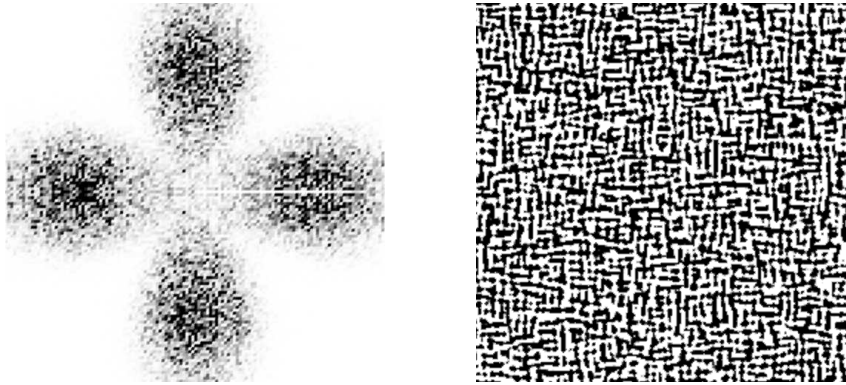
Fig. 3.2. Cubic anisotropy of the elasticity tensor; modulus of the Fourier coefficient (left) and sign of the concentration difference c (right)

follow a direction. In fact typical solutions look like in Fig. 1.1 to the left (see [GMW03] for more details). We also refer to [GMW03] for the proof of a theorem which roughly speaking says that with a probability close to one, the evolution to initial data which are randomly chosen out of a neighborhood of a uniform state will be dominated by an invariant manifold which is tangential to the most unstable eigenfunctions of the linearized operator.

4 Numerical approximation of the Cahn–Larché system

The Cahn–Larché system has a variational structure and hence it is natural to use a finite element method for the discretization. The formulation of the

Cahn–Larché system (2.4)–(2.6) is of second order in space and we will use continuous piecewise affine elements to approximate c, w and u.

For a polyhedral domain Ω we choose a quasi-uniform family $\{\mathcal{T}^h\}_{h>0}$ of partitionings of Ω into disjoint simplices with maximal element size $h := \max_{s\in\mathcal{T}^h}\{\text{diam}\,s\}$, so that $\overline{\Omega} = \bigcup_{s\in\mathcal{T}^h} \overline{s}$. Associated to $\mathcal{T}^h$ is the finite element space of continuous piecewise affine elements

$$S^h := \{\varphi \in C^0(\overline{\Omega}) \mid \varphi_{|s} \text{ is linear for all } s \in \mathcal{T}^h\} \subset H^1(\Omega).$$

To formulate a finite element discretization we introduce the lumped mass scalar product $(\cdot, \cdot)^h$ instead of the L^2 scalar product $(\cdot, \cdot)$ as follows: For $v_1, v_2 \in C^0(\overline{\Omega})$ let

$$(v_1, v_2)^h := \int_\Omega \pi^h(v_1 v_2)$$

where $\pi^h : C^0(\overline{\Omega}) \to S^h$ is the interpolation operator, such that $(\pi^h \eta)(p) = \eta(p)$ for all nodes of $\mathcal{T}^h$.

Then a semi-implicit scheme for (2.4)–(2.6) reads as follows.

We search for $c^h, w^h : [0, T] \to S^h$ and $u^h : [0, T] \to (S^h)^d$ such that

$$(\partial_t c^h, \varphi^h)^h = -(\nabla w^h, \nabla \varphi^h), \tag{4.1}$$
$$(w^h, \varphi^h)^h = \gamma(\nabla c^h, \nabla \varphi^h) + (\psi'(c^h), \varphi^h)^h + (W_{,c}(c^h, \nabla u^h), \varphi^h), \tag{4.2}$$
$$0 = (\varepsilon(\nabla u^h) - \overline{\varepsilon}(c^h), C(c^h)\varepsilon(\nabla \xi^h)) \tag{4.3}$$

holds for all $\varphi^h \in S^h, \xi^h \in (S^h)^d$ and all $t \in [0, T]$.

In order to obtain a fully discrete scheme one needs to introduce a time discretization. The simplest implicit time discretization is the implicit Euler scheme in which the time derivative in (4.1) is discretized in the following way

$$(\partial_t c^h, \varphi^h)^h \rightsquigarrow \left(\frac{c_n^h - c_{n-1}^h}{\tau_n}, \varphi^h\right)^h.$$

Here we divided the time interval $[0, T]$ into N steps with length τ_n and set $t_n := \sum_{i=1}^n \tau_i$. The discrete solution at time t_n is denoted by (c_n^h, w_n^h, u_n^h). The resulting numerical scheme has been analyzed in [GRW01, GW05]. In [GRW01] optimal error estimates have been shown in the case that C does not depend on the concentration (homogeneous elasticity). In the case of inhomogeneous elasticity a convergence proof has been given in [GW05].

The fully discrete scheme has the properties that mass is conserved and that the total discrete free energy decreases (see [GRW01, GW05]). The last observation is a consequence of the fact that the discrete problem reflects the gradient flow property of the continuous problem and this is an important fact in the analysis of the scheme (see [GW05]).

It turns out that the so-called Θ-scheme [BGP87, MU94] leads to a more efficient but hard to analyze time discretization. All the computations presented in the following are with the help of the Θ-scheme, but we made sure that computations with the implicit Euler scheme lead to qualitatively similar results

although with higher computational effort. We consider adaptive triangular grids in space and a corresponding a posteriori error control [GRW01, GW05]. The discrete linear systems were solved with the help of the BICG and GM-RES algorithms and for the nonlinear discrete problem we used Newton's method (see [GRW01, GW05] for more details).

Another approach to solve the Cahn–Larché system numerically uses spectral methods. We refer e.g. to the work of Dreyer and Müller [DM00] and Leo, Lowengrub and Jou [LLJ98] and the references therein. Due to the nonlinear structure of the Cahn–Larché system, approaches based on spectral methods loose their efficiency. This is in particular true in the case where the elastic constants are different in the two phases (inhomogeneous elasticity).

To conclude this section we report on some numerical simulations with the above robust and efficient numerical method. We have studied various qualitative effects of the Cahn–Larché model including homogeneous elasticity. We observe e.g. the following (see also [LLJ98])

- particles align their faces to the elastically soft directions of the material (see Fig. 1.2),
- particles align in rows (see Fig. 4.1),
- always the harder phase forms particles in the softer phase independent of the volume fraction (see Fig. 4.2),
- in the case of inhomogeneous elasticity one observes that particles do not merge when close to each other but instead repel each other (see Fig. 4.3).
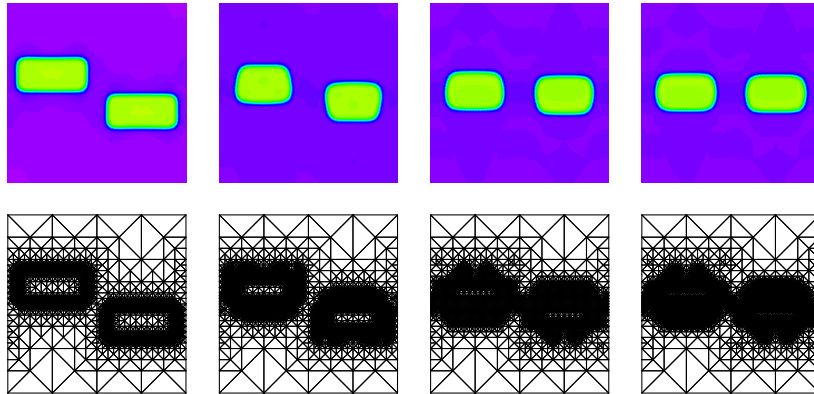

Fig. 4.1. Alignment of two particles (anisotropic inhomogeneous elasticity), adaptive computational grids

The numerical approach for the Cahn–Larché model turns out to be efficient for ensembles ranging from a couple of particles to a few thousand particles and has been applied to derive experimental results on growth laws (see the following section).
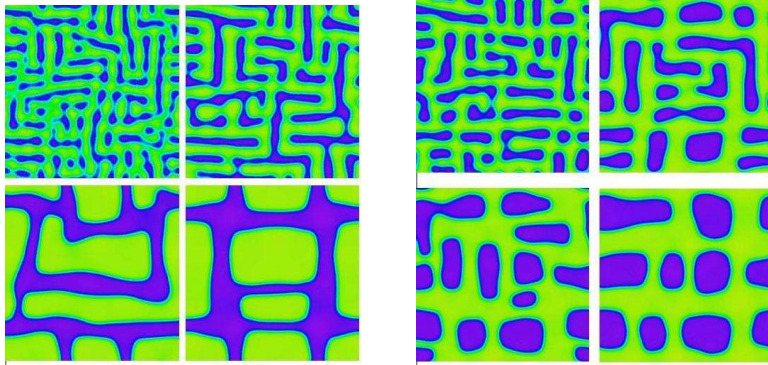
Fig. 4.2. Effects of inhomogeneous elasticity: On the left side the green phase is the elastically harder one, the blue phase is softer. On the right side it is vice versa. The volume fraction of both phases are the same
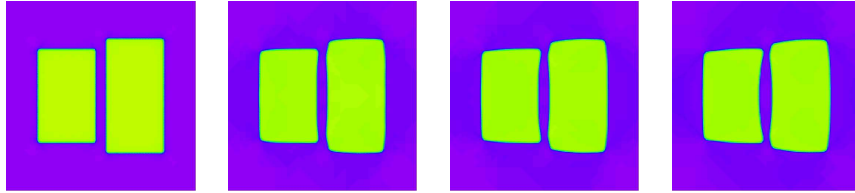
Fig. 4.3. Repulsion of two particles due to anisotropic elasticity

5 Ostwald ripening within the Cahn–Hilliard and Cahn–Larché models

A relevant issue in coarsening systems is an estimate of the coarsening rate of the system. The latter can be expressed by the rate of growth of mean particle size or by the rate of decrease of surface energy. Dimensional arguments give, that the coarsening rate in diffusion controlled coarsening, as described by the Cahn–Hilliard equation or the Mullins–Sekerka evolution, is proportional to $t^{1/3}$. Weak time-averaged upper estimates of this coarsening rate have been established in [KO02] for the Cahn–Hilliard model without elasticity. It turns out that the proof goes through without any difference for the Cahn–Hilliard equation with elasticity. Whether or not this estimate is sharp, say, for generic data, in the case with elasticity is however not clear.

Using the adaptive finite element method described in Sect. 4 we made an attempt to study coarsening rates for large particle systems. We first considered the Cahn–Hilliard model without elasticity. Due to the adaptive grids (see Fig. 4.1) and the time discretization based on the Θ-scheme simulations with about 4000 particles after the initial phase of the particle formation

have been feasible. Let us give a brief summary of the results for the original Cahn–Hilliard model without elasticity (details can be found in [GNRW03]):

- The observed decay rates for the energy and the growth of the averaged particle size are in correspondence with the basic LSW theory. There in 2D one has a decay of the energy like:

$$E = Ct^{-\frac{1}{3}} \,.$$

- Depending on the initial data (arbitrary distributed small particles (cf. Küpper, Masbaum [MK94]), a slightly perturbed homogeneous mixture, a homogeneous mixture with arbitrary positioned localized seeds for particles) we observe a rather long intermediate behaviour with energy decay and particle growth rates different from the expectations.

Figure 5.1 shows results obtained by our extensive numerical tests. On the left the energy is plotted in double logarithmic scale over time. In this representation the expected polynomial decay should turn out as a straight line. This is the case albeit with the unexpected exponent of $-\frac{1}{6}$. In fact, we made the observation that after spinodal decomposition the system settles for a wrong exponent for quite long time. Depending on the volume fractions of the two phases the exponents observed range from $-\frac{1}{6}$ to the expected $-\frac{1}{3}$ in the case where we start with equal volume fractions (see Figure 5.1 upper left graph). However, after a long time the speed of the energy decay changes and we see a behaviour in line with the expectations. In the example shown the energy decay at times $t > 7$ differs significantly from the behaviour at earlier times. We observe a graph like in the left lower part of Fig. 5.1. Here we see time phases where the energy goes according to

$$E \approx Ct^{-\frac{1}{3}}$$

which are intersected by short periods, when the energy decays faster. In these short periods one sees particles vanishing, whereas between these steeper declines particles are just growing and shrinking with the number of particles constant.

In the case of the Cahn–Larché model with elasticity we have observed so far, that the coarsening rates are affected by the presence or absence of elasticity as well as by the homogeneity of the elasticity. Anisotropy seems to play a minor role (cf. Fig. 5.2). However, it may be the case that the coarsening rates change at later times as in the standard Cahn–Hilliard model.
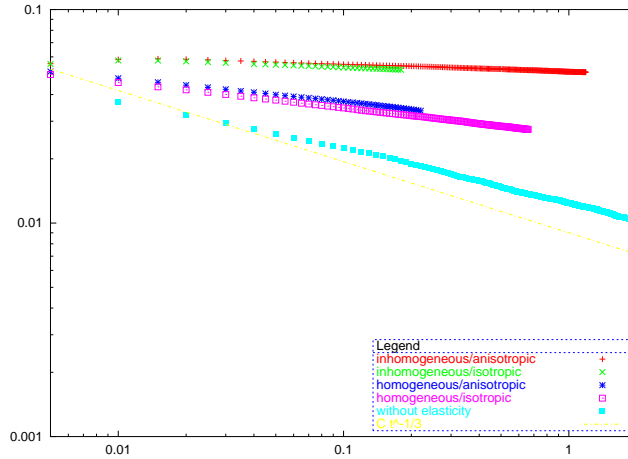
6 Simulation of the sharp interface model

Different from the diffuse interface model which allows a straightforward discretization via finite elements (cf. Sect. 4) the interface propagation in the
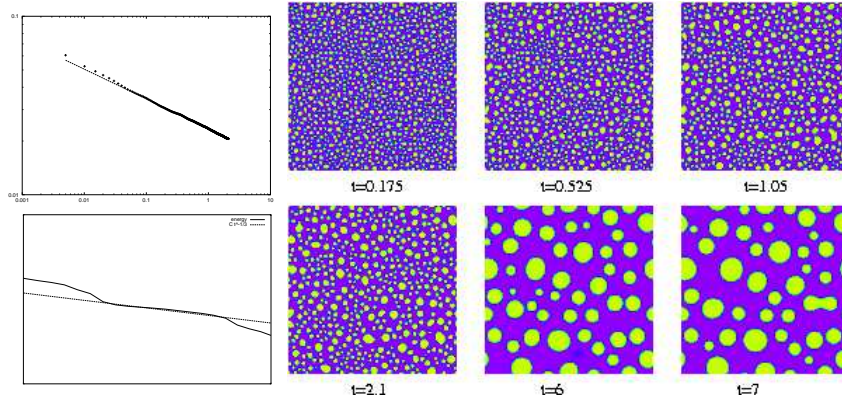
Fig. 5.1. Graph of the energy at an early and a very late stage of the evolution (two graphs on the left side), different time steps of the evolution (on the right side)

Fig. 5.2. Graph of the nonelastic part of the energy

Mullins–Sekerka sharp interface model (2.9)–(2.14) and the computation of the corresponding energy contributions and their variations has preferably been implemented using the boundary element approach. Hence, the linear elliptic subproblems for the chemical potential (2.10),(2.11) and the elastic displacement (2.13),(2.14) are transformed into integral equations on the interface between the different phases. They are then dicretized based on a collocation-type ansatz. Thus, for $d = 2$ the interfaces are resolved by polygonal lines whose vertex positions are updated in the actual evolution. The two dimensional, evolving phase domains have not to be meshed and adapted in each time step of the evolution. Indeed the interface geometry enters the for-

mulation via appropriate Poisson type kernel functions and kernel functions for linear, anisotropic elasticity to be integrated in the collocation ansatz on the polygonal lines [Ha95]. In each time step only the vertex positions representing the interface have to be updated. This discretization approach has among others already been successfully applied by Voorhees, Lowengrub and coworkers [ATV01, JLL97, TAV04a, TAV04b, VMJ92].

Let us first depict this transformation for the chemical potential subproblem. Let $\psi_{x_0}(x) := -\frac{1}{2\pi} \ln |x - x_0|$ be the fundamental solution for the Laplacian in $\mathbf{R}^2$, i.e. $\Delta\psi_{x_0}(x) = \delta(x - x_0)$ in the sense of distributions. Applying Greens formula we obtain for points x_0 on a smooth interface Γ:

$$\mu(x_0) = \int_\Gamma \{[\mu]\,(x)\partial_\nu\psi_{x_0}(x) - \psi_{x_0}(x)\,[\partial_\nu\mu]\,(x)\}\,dx$$

$$+ \int_{\partial B_R} \{\mu(x)\partial_{\tilde\nu}\psi_{x_0}(x) - \psi_{x_0}(x)\partial_{\tilde\nu}\mu(x)\}\,dx\,.$$

Here, μ is the chemical potential, $[\cdot]$ the usual jump operator and B_R is a large ball containing all particles. Recalling that μ is continuous across the interface (2.11) the jump of the chemical potential $[\mu]$ vanishes. Furthermore, for $R \to \infty$ the integral over ∂B_R converges to a constant $c(t)$ solely depending on time. This additional degree of freedom reflects the conservation of the overall particle volume. Finally taking into account the governing equation for the normal velocity of the interface (2.9) the Mullins–Sekerka problem can be rewritten in the following form:

Let $\Gamma(t)$ be the interface with normal velocity v, κ its curvature, and $E = E(\chi, \nabla u)$ the Eshelby tensor (2.12), then at time t

$$\kappa(x_0, t) + [E(x_0, t)]\nu(x_0, t) \cdot \nu(x_0, t) + c(t) = \int_{\Gamma(t)} \psi_{x_0}(x)v(x, t)\,d\mathcal{H}^1 \quad (6.1)$$

for every x_0 on $\Gamma(t)$ and the velocity field fulfills the constraint $0 = \int_{\Gamma(t)} v\,d\mathcal{H}^1$.

The solution of the quasi stationary elastic subproblem is required for the evaluation of the Eshelby tensor E on Γ. Let C_α be the elasticity tensor, where the index α indicates either the matrix or the particle phase, and denote by $\bar\epsilon_\alpha$ the misfit. Let u be the displacement on the interface and τ the normal stress defined as the difference between actual strain and eigenstrain in normal direction: $\tau = \sigma\nu = C(\epsilon(\nabla u) - \bar\epsilon_\alpha)\nu$. We recall from (2.14) that τ is continuous across the interface. Now we consider the matrix valued fundamental solutions $\psi_{x_0}^\alpha$ for linear, anisotropic elasticity from [CR78, Cle87] and obtain again by Greens formula an integral equation

$$\frac{1}{2}u(x_0) = \int_\Gamma \partial_{C_\alpha\nu}\psi_{x_0}^\alpha(x)u(x) - \psi_{x_0}^\alpha(x)\,(\tau(x) + C_\alpha\bar\epsilon_\alpha\nu)\,d\mathcal{H}^1\,.$$

Let us remark that in case x_0 coincides with a vertex on a polygonal interface, a matrix $c(x_0)$ depending on the direction of the two edges at x_0 is applied

to the displacement $u(x_0)$ on the left hand side replacing the factor $\frac{1}{2}$. Given the above integral equation for the matrix and for the particle phase, the displacement u and the normal stress τ are up to a constant displacement uniquely determined. The computation of the Eshelby tensor requires the evaluation of the full displacement gradient ∇u. For given u and τ this gradient can be computed differentiating the above integral equation with respect to x_0. This differentiation applies to the integral kernels, thus increasing the order of singularity. In particular, for the kernel $\partial_{C_\alpha \nu} \psi_{x_0}^\alpha$ a hypersingular integral has to be evaluated.

In the actual spatial discretization the integral equations are assumed to be fulfilled at appropriate collocation points on a polygonal interface and the displacement, the normal stresses, the chemical potential, and the interface velocity are approximated in a corresponding discrete space. Two particular useful choices are either piecewise constant ansatz functions on the polygon segments and segment centers as collocation points, or a piecewise linear functions and vertices as collocation points. For the elastic subproblem, piecewise linear ansatz functions are the appropriate choice, since piecewise constant ansatz functions do not make sense with respect to the above sketched evaluation of the deformation gradient on the interface.

For the notion of a discrete curvature on the polygonal interface we refer to [Dz91] and define on vertex x_i a curvature vector

$$\kappa_i \nu_i := - \frac{\frac{x_{i+1}-x_i}{\|x_{i+1}-x_i\|} - \frac{x_i-x_{i-1}}{\|x_i-x_{i-1}\|}}{\frac{\|x_{i+1}-x_i\|+\|x_i-x_{i-1}\|}{2}} \, , \tag{6.2}$$

where ν_i represents a unit length vector and κ_i the discrete, scalar curvature required for a spatially discrete Mullins–Sekerka model. Finally, a suitable time discretization for (6.1) has to be considered. An explicit treatment of the discrete curvatures κ_i would result in severe time step restrictions. Thus, we evaluate the normal direction – according to the above equation – at the old time step and redefine a semi-implicit scalar curvature as the scalar product of this time explicit normal field with a semi-implicit curvature vector. For the latter, we again follow [Dz91] and consider time implicit vertex positions but a time explicit edge length in the above formula (6.2).

Let us depict two types of particle interaction in the presence of inhomogeneous and anisotropic elasticity. Figure 6.1 shows the attraction of particles in case of a strongly inhomogeneous elasticity with a hard particle phase and a considerably softer matrix phase. Figure 6.2 renders the alignment of particles, which can be observed in the presence of strongly anisotropic elasticity.

7 Reduced sharp interface model for larger systems

In order to make simulations for large particle systems feasible, we now set up a reduced model of the Mullins–Sekerka evolution with elasticity. The re-
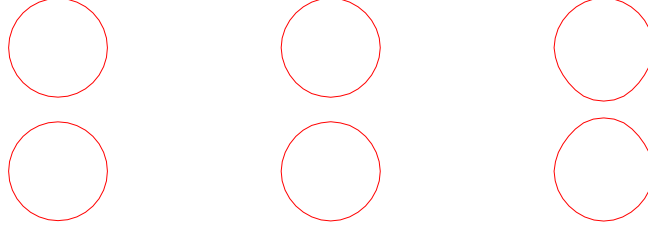
Fig. 6.1. Three time steps of a discrete Mullins–Sekerka evolution showing the attraction of two soft particles in case of isotropic but inhomogeneous elasticity. The matrix phase is four times harder than the particle phase
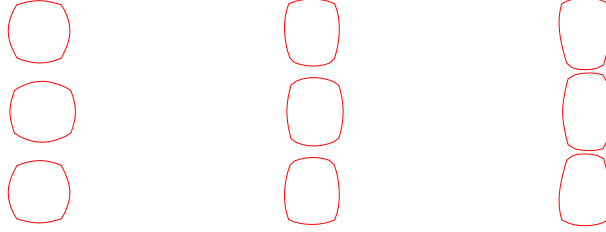
Fig. 6.2. Three time steps of a discrete Mullins–Sekerka evolution with particles lining up

duction is based on the observation that in the case of a cubic anisotropy in the elasticity, particles become quickly rectangular, whereas the long-time behavior is dominated by long-range interactions. This motivates to reduce the gradient flow of the Mullins–Sekerka evolution to the submanifold of rectangular particles. We will see, that such a reduction is in very good agreement with the full evolution for a small set of particles. We will then also present first results for larger particle ensembles.

We restrict our dynamical system to the submanifold $\mathcal{N} \subset \mathcal{M}$ which consists of sets which are the union of disjoint rectangular particles aligned with the coordinate axes.

To define $\mathcal{N}$ we first need to introduce some notation. As indicated in Fig. 7.1 each particle will be identified by the two points

$$p = (p^-, p^+) = ((p_x^-, p_y^-), (p_x^+, p_y^+)) \in \mathbf{R}^2 \times \mathbf{R}^2.$$

We denote the edges perpendicular to the x-axes by b_x^- and b_x^+, the ones perpendicular to the y-axes by b_y^- and b_y^+, more precisely $b_x^- := \{p_x^-\} \times [p_y^-, p_y^+], b_x^+ := \{p_x^+\} \times [p_y^-, p_y^+]$ and $b_y^- := [p_x^-, p_x^+] \times \{p_y^-\}, b_y^+ := [p_x^-, p_x^+] \times \{p_y^+\}$. Consequently the volume of a particle p is given by $a_p = |b_x^-| \cdot |b_y^-|$ and the boundary length by $l_p := |b_x^-| + |b_y^-| + |b_x^+| + |b_y^+|$.

v_y^+ $p^+ = (p_x^+, p_y^+)$

v_x^- v_x^+

$p^- = (p_x^-, p_y^-)$ v_y^-
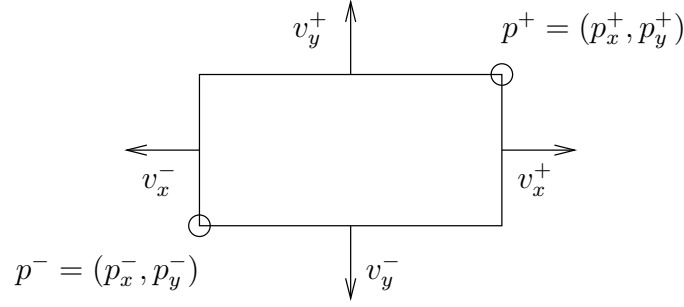
Fig. 7.1. Configuration of one rectangular, axis-aligned particle

The normal velocities of the sides are given by

$$v_p = (v_x^-, v_x^+, v_y^-, v_y^+) \in \mathbf{R}^4.$$

Now our submanifold $\mathcal{N}$ can be identified with the space

$$\mathcal{N} := \left\{ \mathbf{P} = \{p_i\}_i, i = 1, \ldots, N \,\middle|\, \sum_{p_i} a_{p_i} = \mathcal{V} \right\} \subset \mathbf{R}^{4N},$$

where N is the number of particles, and the tangent space with the hyperplane

$$T_{\mathbf{P}}\mathcal{N} := \left\{ \mathbf{V} = \{v_i\}_i, i = 1, \ldots, N \,\middle|\, \begin{array}{l} \sum_i \left(|b_x^-|((v_i)_y^- + (v_i)_y^+) \right. \\ \left. + |b_y^-|((v_i)_x^- + (v_i)_x^+) \right) = 0 \end{array} \right\}.$$

The surface energy $\tilde{\mathcal{E}}$ can be expressed as

$$\tilde{\mathcal{E}} = \int |\nabla \chi| = 2 \sum_i \left(|(b_i)_x^-| + |(b_i)_y^+| \right),$$

such that the variation of $\tilde{\mathcal{E}}$ with respect to $\tilde{v} \in T_p\mathcal{N}$ is given by

$$\langle \mathrm{diff}\tilde{\mathcal{E}}, \tilde{v} \rangle = 2 \sum_i \left((\tilde{v}_i)_x^- + (\tilde{v}_i)_x^+ + (\tilde{v}_i)_y^- + (\tilde{v}_i)_y^+ \right). \qquad (7.1)$$

We are now going to consider what interfacial condition is satisfied for the direction of steepest descent as given in (2.17). For that notice that we can for any vector $w \in \mathbf{R}^{4n}$ construct an element $\tilde{v} \in T_p\mathcal{N}$ by setting

$$\tilde{v}_i = w_i - \frac{\sum_j (w_j b_j)_x^- + (w_j b_j)_x^+ + (w_j b_j)_y^- + (w_j b_j)_y^+}{\sum_j l_{p_j}} =: w_i - \bar{w}.$$

Using (2.17) and (7.1) we easily find that there is a constant C such that for all $i \in 1, \ldots, N$ we have

$$\fint_{(b_i)_\alpha^\beta} \mu \, d\mathcal{H}^1 = \frac{2}{|(b_i)_\alpha^\beta|} + \fint_{(b_i)_\alpha^\beta} [E_{(b_i)_\alpha^\beta}] \, d\mathcal{H}^1 + C \qquad (7.2)$$

where $\alpha = x, y$, $\beta = +, -$, $i = 1, \ldots, N$, $[E_b] := [E(\chi, \nabla u)] : \nu_b \nu_b^T$ and $\fint_b := \frac{1}{|b|} \int_b$, where $E(\chi, \nabla u)$ is the Eshelby tensor from (2.12). The term $\frac{2}{|(b_i)_\alpha^\beta|}$ can be interpreted as a crystalline curvature which also appears for surface energies with cubic crystalline anisotropy (see e.g. Taylor [Tay78] and Gurtin [Gu93]).

We summarize the above to define the evolution in the restricted setting. This will also motivate the order in which the equations are evaluated in the numerical algorithm.

For a given particle configuration $\mathbf{P} = \{p_i : i = 1, \ldots, N\}$ we compute in view of (2.13), (2.14) the elastic deformation u from

$$\operatorname{div} \frac{\partial W}{\partial F}(\chi, \nabla u) = 0 \qquad \text{in } \mathbf{R}^2 \backslash \Gamma,$$

$$[u] = \left[\frac{\partial W}{\partial F}(\chi, \nabla u) \cdot \nu \right] = 0 \qquad \text{on } \Gamma := \bigcup_{i, \alpha, \beta} (b_i)_\alpha^\beta$$

for $\alpha = x, y$, $\beta = +, -$, $i = 1, \ldots, N$. The chemical potential μ is given (cf. (2.15) and (7.2)) by

$$\Delta \mu = 0 \qquad \qquad \text{in } \quad \mathbf{R}^2 \backslash \Gamma,$$

$$\fint_{(b_i)_\alpha^\beta} \mu \, d\mathcal{H}^1 = \frac{2}{|(b_i)_\alpha^\beta|} + \fint_{(b_i)_\alpha^\beta} [E_{(b_i)_\alpha^\beta}] \, d\mathcal{H}^1 + C$$

for $\alpha = x, y$, $\beta = +, -$ and $i = 1, \ldots, N$, so that the velocities can be derived from (2.16) via

$$(v_i)_\alpha^\beta = -[\partial_{\nu_{(b_i)_\alpha^\beta}} \mu] \qquad \text{for } \alpha = x, y, \ \beta = +, -, \ i = 1, \ldots, N.$$

This evolution is well-defined until the side of a particle shrinks to zero. Then we remove this particle and continue with the remaining particles.

To compare the reduced model to the full Mullins–Sekerka evolution, we simulate the interaction of a group of particles. Indeed, from a start configuration for the full model, we compute a couple of small time steps to allow the particle shapes to relax to their preferred form (which happens rather quickly). For this configuration of nearly rectangular particles we construct a matching starting configuration for the reduced model. This configuration is then considered as the initial data both for the reduced and the full model. In both models particles below a certain small diameter are deleted completely. Figure 7.2 shows computational results for both models at different time steps of the evolution. The corresponding evolution of the interfacial energy over time is depicted in Fig. 7.3. Furthermore, plots of the elastic strain,
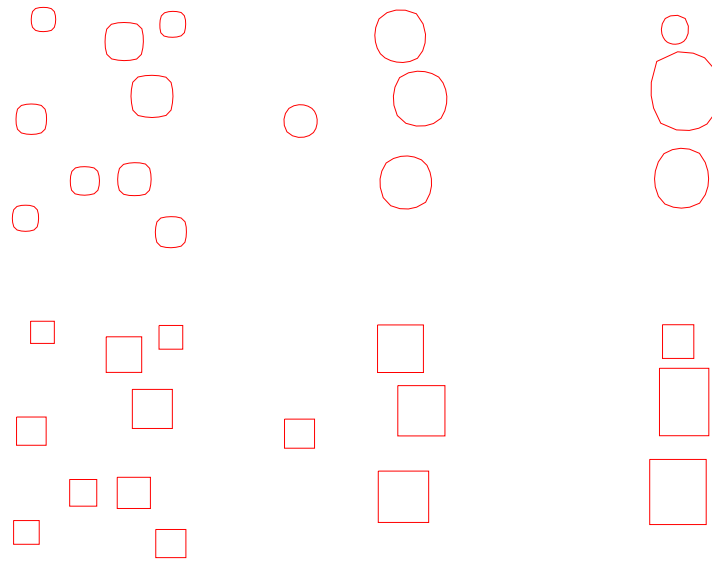
Fig. 7.2. Evolution of the interface for the full Mullins–Sekerka model (top) and for the reduced model (bottom). In both case the time steps $t = 0; 0.0011; 0.004$ are depicted
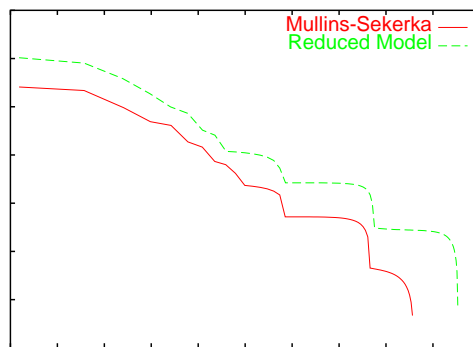

Fig. 7.3. The evolution of the interfacial energy is rendered for both models. Time and energy axis are logarithmic

stress and the energy density are compared in Fig. 7.4. Indeed, one observes a striking qualitative similarity and basically the same temporal behaviour. Finally, time steps from the evolution of a moderately large particle ensemble with about one thousand particles and homogeneous anisotropic elasticity are shown in Fig. 7.5.

References

[ATV01]   N. Akaiwa, K. Thornton, and P.W. Voorhees. Large–Scale Simulations of Microstructural Evolution in Elastically Stressed Solids. *J. Comp. Phys.*, 173, 61–86, 2001.

[BGP87]   M.O. Bristeau, R. Glowinski, and J. Periaux. Numerical methods for the Navier-Stokes equations: Applications to the simulation of compressible and incompressible viscous flows. In: Computer Physics Report, Research Report UH/MD-4. University of Houston, 1987.

[CH58]   J.W. Cahn and J.E. Hilliard. Free energy of a nonuniform system. I. Interfacial free energy. *Journal of Chemical Physics*, 28, 258–267, 1958.

[CL73]   J.W. Cahn and F.C. Larché. A linear theory of thermomechanical equilibrium of solids under stress. *Acta Metall.*, 21, 1051–1063, 1973.

[CL82]   J.W. Cahn and F.C. Larché. Surface stress and the chemical equilibrium of single crystals II: solid particles imbedded in a solid matrix. *Acta Metall.*, 30, 51–56, 1982.

[Cle87]   D.L. Clements. Green's Functions for the Boundary Element Method. *Boundary Elements IX: Proceedings of the 9th International Conference on Boundary Elements*, 1987.

[CR78]   D.L. Clements and F.J. Rizzo. A Method for the Numerical Solution of Boundary Value Problems Governed by Second-Order Elliptic Systems. *J. Inst. Math. Appl.*, 22, 197–202, 1978.

[DM00]   W. Dreyer and W.H. Müller. A study of the coarsening in tin/lead solders. *Int. J. Solids Struct.*, 37, 381–3871 , 2000.

[Dz91]   G. Dziuk. An algorithm for evolutionary surfaces. *Numer. Math.*, 58, 603–611, 1991.

[Ell89]   C.M. Elliott The Cahn-Hilliard model for the kinetics of phase transitions, in Mathematical Models for Phase Change Problems, J.F. Rodrigues (ed.). *International Series of Numerical Mathematics*, 88, Birkhäuser-Verlag, Basel, 35–73, 1989.

[FPL99]   P. Fratzl, O. Penrose, and J.L. Lebowitz. Modelling of phase separation in alloys with coherent elastic misfit. *J. Stat. Physics*, 95 5/6, 1429–1503, 1999.

[Ga03a]   H. Garcke. On Mathematical Models for Phase Separation in Elastically Stressed Solids. Habilitation Thesis 2003

[Ga03b]   H. Garcke. On Cahn-Hilliard systems with elasticity. *Proc. Roy. Soc. Edinburgh*, 133 A, 307–331, 2003.

[GK06]   H. Garcke and D.J.C. Kwak. On asymptotic limits of Cahn-Hilliard systems with elastic misfit. contribution to this book.

[GMW03]   H. Garcke, S. Maier-Paape, and U. Weikard. Spinodal decomposition in the presence of elastic interactions. appeared in S. Hildebrand,
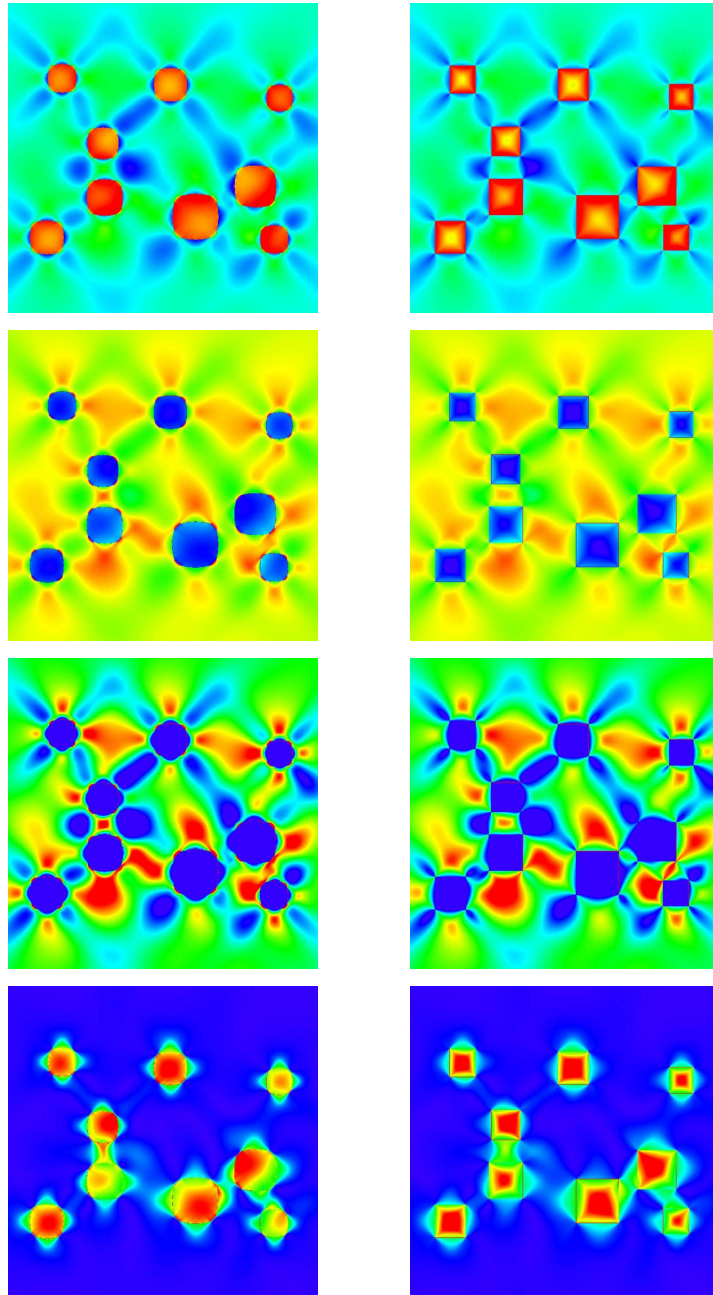
Fig. 7.4. The trace of the elastic strain (both top rows, compared to zero strain and eigenstrain), the trace of the stress (middle) and energy density (bottom) for the Mullins–Sekerka (left) and the reduced model (right), in the initial configuration
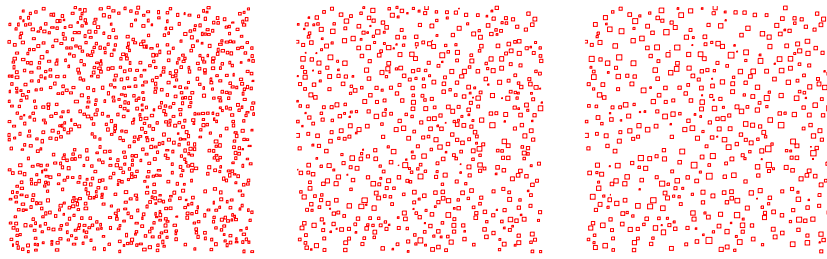
Fig. 7.5. Coarsening of a moderately large particle ensemble

H. Karcher (Eds.), *Geometric Analysis and Nonlinear Partial Differential Equations,* Springer, 2003.

[GNRW03] H. Garcke, B. Niethammer, M. Rumpf, and U. Weikard. Transient coarsening behaviour in the Cahn-Hilliard model *Acta Mat.*, 51, 2823–2830, 2003.

[GRW01] H. Garcke, M. Rumpf, and U. Weikard, The Cahn-Hilliard equation with elasticity: Finite element approximation and qualitative studies. *Interfaces and Free Boundaries*, 3, pp. 101–118, 2001.

[GW05] H. Garcke and U. Weikard. Numerical Approximation of the Cahn-Larché equation. *Numer. Math.*, 100, Number 4, 639–662, 2005.

[Gu72] M.E. Gurtin. The Linear Theory of Elasticity. *Handbuch der Physik*, Vol. VIa/2, Springer, S. Flügge and C. Truesdell (eds.), Berlin, 1972.

[Gu93] M.E. Gurtin. *Thermomechanics of evolving phase boundaries in the plane.* Oxford Mathematical Monographs. New York, 1993.

[Ha95] W. Hackbusch. *Integral Equations. Theory and Numerical Treatment.* Birkhäuser 1995.

[JLL97] H.-J. Jou, P.H. Leo, and J.S. Lowengrub. Microstructural Evolution in Inhomogeneous Elastic Media. *J. Comp. Phys.*, 132, 109–148, 1997.

[Kha83] A.G. Khachaturyan. *Theory of Structural Transformations in Solids.* Wiley, New York, 1983.

[KO02] R.V. Kohn and F. Otto. Upper bounds for coarsening rates. *Comm. Math. Phys.*, 229, 375–395, 2002.

[LLJ98] P.H. Leo, J.S. Lowengrub, and H.J. Jou. A diffuse interface model for microstructural evolution in elastically stressed solids. *Acta Mater.*, 46, 2113–2130, 1998.

[MK94] N. Masbaum and T. Küpper. Simulation of particle growth and Ostwald ripening via the Cahn-Hilliard equation. *Acta Metallurgica et Materialia*, 42, No.6, 1847–1858, 1994.

[MU94] S. Müller-Urbaniak. Eine Analyse des Zwischenschritt-θ-Verfahrens zur Lösung der instationären Navier-Stokes-Gleichungen. Preprint 94-01 des SF 359, 1994.

[Pe89] R.L. Pego. Front migration in the nonlinear Cahn-Hilliard equation. *Proc. Roy. Soc. London*, Ser. A 422, no. 1863, 261–278, 1989.

[Tay78] J.E. Taylor. Crystalline variational problems. *Bull. Amer. Math. Soc.*, 84 (4), 568–588, 1978.

[TAV04a]   K. Thornton, N. Akaiwa, and P.W. Voorhees. Large-scale simulations
of Ostwald ripening in elastically stressed solids. I. Development of Mi-
crostructure. *Acta Materialia*, 52, 1353–1364, 2004.

[TAV04b]   K. Thornton, N. Akaiwa, and P.W. Voorhees. Large-scale simulations
of Ostwald ripening in elastically stressed solids. II. Coarsening kinetics
and particle size distribution. *Acta Materialia*, 52, 1365–1378, 2004.

[VMJ92]   P.W. Voorhees, G.B. McFadden, and W.C. Johnson. On the morpholog-
ical development of second phase particles in elastically stressed solids.
Acta Metall., 40, 2979–2992, 1992.

[Wei02]   U. Weikard. Numerische Lösungen der Cahn-Hilliard-Gleichung und
der Cahn-Larché-Gleichung. PhD thesis, Bonn, 2002.